Geochemistry Geophysics Geosystems G3
AN ELECTRONIC JOURNAL OF THE EARTH SCIENCES
Published by AGU and the Geochemical Society

Article
Volume 7, Number 2
10 February 2006
Q02006, doi:10.1029/2005GC001071
ISSN: 1525-2027

Dynamics of thermochemical plumes: 1. Plume formation and entrainment of a dense layer

Shu-Chuan Lin

Department of Geological Sciences, University of Michigan, 2534 C. C. Little Building, 1100 North University, Ann Arbor, Michigan 48109, USA

Now at Department of Geosciences, National Taiwan University, 1, Section 4, Roosevelt Road, Taipei 106, Taiwan (skylin0@ntu.edu.tw)

Peter E. van Keken

Department of Geological Sciences, University of Michigan, 2534 C. C. Little Building, 1100 North University, Ann Arbor, Michigan 48109, USA (keken@umich.edu)

[1] Density variations due to changes in bulk chemistry in the lowermost mantle play an important role in the dynamics and chemistry of plumes. In this study we perform a series of high-resolution numerical experiments in an axisymmetric spherical shell to systematically investigate the formation of plumes from a thermochemical boundary layer and the entrainment of the dense material by plumes. In particular, we investigate the effects of the temperature dependence of viscosity, the chemical density contrast, and thickness of the compositionally distinct layer. Our results show that all three factors influence the nature of plume formation and entrainment of dense material. The complexity of the evolution of the plumes and of the entrainment process increases profoundly with increasing viscosity contrast. The entrainment commonly becomes a transient process for models with variable viscosity. It is generally stronger in the isoviscous models, but the development of plumes is easier in the models with variable viscosity, which is mainly determined by the mechanical coupling between the dense material and the surrounding mantle. Our model results indicate that the compositionally distinct region in D″ can survive in the Earth's history if the intrinsic density contrast of the compositionally distinct layer is greater than about 2%. We also present a series of benchmark tests for thermochemical convection problems in an axisymmetric spherical shell. Our tests indicate that high-resolution models are necessary for the thermochemical convection systems in which strongly temperature-dependent viscosity is considered.

Components: 3397 words, 18 figures, 1 table.

Keywords: mantle convection; thermochemical plumes; D″; entrainment; axisymmetric spherical shell.

Index Terms: 8121 Tectonophysics: Dynamics: convection currents, and mantle plumes; 8194 Tectonophysics: Instruments and techniques.

Received 13 July 2005; **Revised** 21 September 2005; **Accepted** 11 November 2005; **Published** 10 February 2006.

Lin, S.-C., and P. E. van Keken (2006), Dynamics of thermochemical plumes: 1. Plume formation and entrainment of a dense layer, *Geochem. Geophys. Geosyst.*, *7*, Q02006, doi:10.1029/2005GC001071.

1. Introduction

[2] The fundamental difference of the isotope ratios between oceanic island basalts (OIBs) and mid-oceanic ridge basalts (MORBs) is conventionally attributed to the long-term isolation of the distinctive chemical reservoirs [e.g., *Depaolo and Wasserburg*, 1976; *Hofmann*, 1997; *Kellogg et al.*, 1999; *van Keken et al.*, 2002]. The nature of these chemical reservoirs in terms of the length scale,

distribution and origin is, however, under debate [e.g., *van der Hilst et al.*, 1997; *Kellogg et al.*, 1999; *Morgan and Morgan*, 1999; *Becker et al.*, 1999; *Tackley*, 2000; *van Keken et al.*, 2002, 2003]. The most significant and perhaps only global deep boundary layer within the mantle is the D″ layer in the lowermost 200–300 kilometer of the mantle. The D″ layer is generally invoked as the source region of mantle plumes with deep origin. Seismic observations reveal the strongly lateral heterogeneities with complicated details in the D″ layer including large-scale features that may extend into the region of 500–1000 km above the core-mantle boundary (CMB) [e.g., *Lay and Helmberger*, 1983; *Dziewonski et al.*, 1993; *Lay et al.*, 1998; *Kuo et al.*, 2000; *Fisher et al.*, 2003; *Hung et al.*, 2005]. The compositionally distinct layer in the lowermost mantle may better explain features that cannot be attributed to thermal effects alone: (1) the decorrelation between the bulk sound and shear wave velocity structures with the horizontal length scale of at least several hundred kilometers in the well sampled regions such as the central Pacific [e.g., *Masters et al.*, 2000; *Lay*, 2005]; (2) the presence of the regional shear wave discontinuity atop D″ layer [e.g., *Wysession et al.*, 1998]; (3) the estimate of large density increase (+10%) of the regional ultra low velocity zones (ULVZs) with a sharp upper boundary located a few tens of kilometers above CMB [e.g., *William and Garnero*, 1996; *Wen et al.*, 2001; *Rost et al.*, 2005]; (4) the sharp boundary of the large low velocity province beneath the southern Atlantic Ocean, Africa and southern Indian Ocean inferred from shear wave and geodynamics studies [e.g., *Ni et al.*, 2002; *Ni and Helmberger*, 2003]; (5) the constraints based on analysis of normal-mode and free-air gravity data [*Ishii and Tromp*, 1999]. The composition, length-scale, physical properties and lateral heterogeneity of this compositional layer are still controversial.

[3] It has been proposed that the compositional layer in the lowermost mantle results from the accumulation of subducted oceanic crust [e.g., *Christensen and Hofmann*, 1994; *van der Hilst et al.*, 1997]. The plumes may entrain the subducted crust and contribute to the diversity of isotope ratios of OIBs [e.g., *Hofmann and White*, 1982; *Lassiter and Hauri*, 1998; *Sobolev et al.*, 2000]. The chemical reaction between core and mantle and partial melting can also increase the material density by iron enrichment [e.g., *Manga and Jeanloz*, 1996; *William and Garnero*, 1996; *Wen et al.*, 2001; *Rost et al.*, 2005]. These mechanisms, along with the differentiation processes of the metallic minerals in a chemical boundary layer at the base of the mantle [e.g., *Manga and Jeanloz*, 1996] may also contribute to the formation of the dense layer in the lowermost mantle. An alternative hypothesis for the compositionally dense layer at the base of the mantle is that it formed during the early differentiation of Earth, by the formation and recycling of a mafic crust in the Archaean, or by processes associated with a deep magma ocean [*Kellogg et al.*, 1999].

[4] Both laboratory and theoretical approaches have been used to investigate the dynamics of the compositionally dense layer in a convecting system. General findings are that dense material is swept toward the upwelling flow rising from the basal thermal boundary layer (TBL) causing a nonuniform thickness of the dense layer and subsequent entrainment of dense material in plumes [e.g., *Christensen and Hofmann*, 1994; *Montague and Kellogg*, 2000; *Jellinek and Manga*, 2002; *Tackley*, 1998, 2002; *Davaille et al.*, 2002; *McNamara and Zhong*, 2004]. If any compositional layer does exist and has persisted in the lowermost mantle for a significant period of time, previous studies suggest its intrinsic density is denser than the overlying mantle in the range of 1%–6% [e.g., *Sleep*, 1988; *Christensen and Hofmann*, 1994; *Montague et al.*, 1998; *Kellogg et al.*, 1999; *Gonnermann et al.*, 2002; *Samuel and Farnetani*, 2003; *Zhong and Hager*, 2003]. The chemical stratification across D″ may be responsible for the discrepancy between the plume excess temperature in the upper mantle (∼200–300 K) and the estimated temperature increase across the TBL (∼1000 K or more) [*Farnetani*, 1997; *Farnetani et al.*, 2002]. *Zhong and Hager* [2003] and *Oldham and Huw Davies* [2004] conclude from isoviscous models that the entrainment is mainly controlled by the radius of the thermal plume and the ratio of compositional to thermal buoyancy, but is relatively insensitive to the thickness of the dense layer. Laboratory experiments have been able to approach the dynamics more systematically, but mainly focused on the longevity and the shape of the chemical layer and its role on the fixity of the plumes in experiments with a thick dense layer ($\sim \geq$300 km) [e.g., *Gonnermann et al.*, 2002] or a dense layer with higher viscosity [e.g., *Davaille*, 1999].

[5] The main purpose of this work is to systematically study the entrainment of a dense layer by plumes and to explore the characteristics of the plumes in a thermochemical convection system by

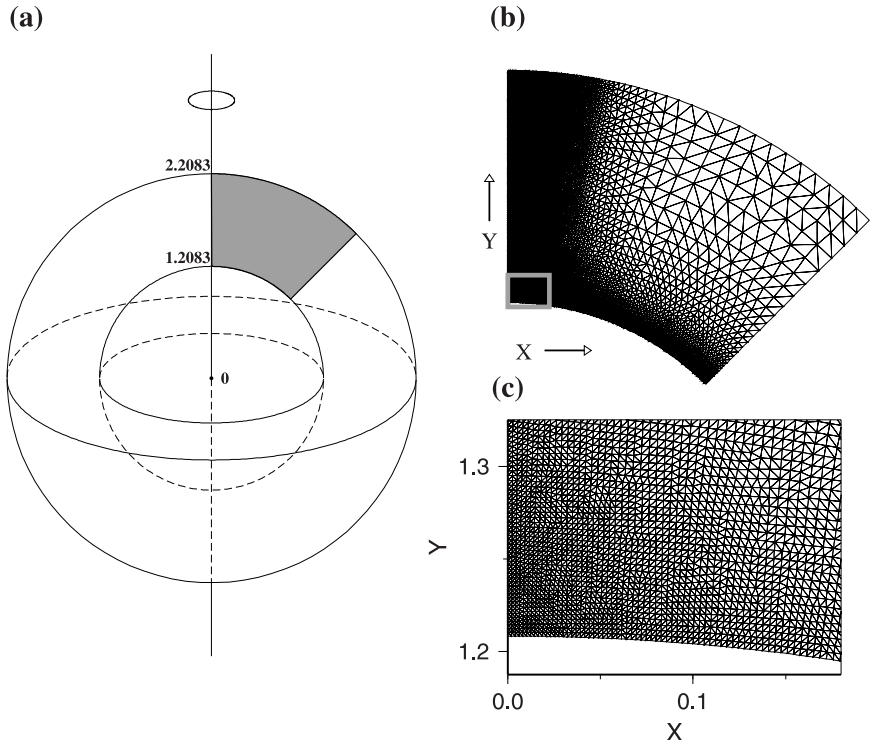

Figure 1. (a) Axisymmetric spherical geometry for finite element models. Segment in gray shows the model domain used in this study. (b) Finite element mesh for high-resolution models in this study. The resolution of the models shown here is ~2–5 km in the regions near the corner of the plume axis and core. (c) A close-up of the mesh near the core and plume axis. Length scale is rescaled by the thickness of the mantle (2885 km).

numerical experiments that cover a wide parameter space. In particular, we focus on a thermochemical boundary layer that is formed by mixing between recycled and dense oceanic crust and ambient mantle. For simplicity we will refer to the recycled oceanic crust as eclogite.

[6] We examine models with a compositionally distinct layer with a compositional excess density $\Delta\rho$ in the lowermost mantle ranging from 0 to 400 kg/m^3 and the initial thickness d ranging from 10 to 200 km. We will consider both isoviscous and temperature-dependent rheology. In the later case we will vary the maximum viscosity contrast ($\Delta\eta$) between ambient mantle and the hottest plume material between 100 and 1000. As shown below our models reveal the complexity of the entrainment process and its influence on plume structure. Both depend strongly on the viscosity contrast as well as the thickness and the excess density of the compositional layer. In the remainder of this paper we will discuss the modeling approach in detail before presenting the results. Ideally, we would like to investigate the dynamics of entrainment from the thermochemical boundary layer using three-dimensional spherical models. Yet, the accurate numerical modeling of thermochemical convection is a daunting task and the use of full three-dimensional calculations is still difficult at present due to limited computational resources [e.g., *van Keken et al.*, 1997; *Tackley*, 2002; *McNamara and Zhong*, 2004]. In order to make a substantial number of highly resolved model studies possible we use an axisymmetric spherical shell geometry (Figure 1) which is an appropriate geometrical simplifications for plume modeling [*Kellogg and King*, 1997]. The use of the finite element method also allows us to use strong grid refinement in the TBL and at the plume axis (Figures 1b and 1c). The general characteristics of the entrainment process and of the plume formation are presented in this paper. More details of the plume structure and the corresponding flow field will be discussed in a companion paper [*Lin and van Keken*, 2006]. A series of tests for the thermochemical convection problems are presented in Appendices A, B, and C.

2. Numerical Models

[7] Our numerical experiments are conducted by considering the thermochemical convection in a

Table 1. Symbols and Dimensional Reference Values

Symbols	Quantity	Value
α	thermal expansivity	3×10^{-5} K^{-1}
ρ_0	reference mantle density	4000 kg m^{-3}
g	gravitational acceleration	9.8 m s^{-2}
κ	thermal diffusivity	10^{-6} m^2 s^{-1}
ΔT	temperature contrast across thermal boundary layer	750 K
h	depth of the mantle	2885 km
η_0	reference mantle viscosity	10^{22} Pa · s

Boussinesq fluid at infinite Prantdl number in an axisymmetric spherical shell geometry. The non-dimensional equations governing the flow can be expressed by the equations of motion,

$$\nabla \cdot (\eta \dot{\epsilon}) - \nabla P = (Ra\, T - Rb\Gamma)\hat{\mathbf{z}} \tag{1}$$

the continuity equation,

$$\nabla \cdot \mathbf{u} = 0 \tag{2}$$

the energy equation,

$$\frac{\partial T}{\partial t} + (\mathbf{u} \cdot \nabla)\, T = \nabla^2 T \tag{3}$$

and the advection equation for composition,

$$\frac{\partial \Gamma}{\partial t} + (\mathbf{u} \cdot \nabla)\, \Gamma = 0 \tag{4}$$

where η is viscosity, $\dot{\epsilon}$ is the deviatoric strain rate tensor, P is the dynamic pressure, $\mathbf{u}$ is velocity, t is time, T is temperature, Γ is the composition function, $\hat{\mathbf{z}}$ is the unit vector in the direction of gravity. Ra and Rb are the thermal and compositional Rayleigh numbers, respectively, and given by

$$Ra = \frac{\alpha \rho_0 g \Delta T h^3}{\kappa \eta_0}, \quad Rb = \frac{\Delta \rho g h^3}{\kappa \eta_0} \tag{5}$$

The definitions and the quantities on the right-hand size are given in Table 1 along with the dimensional values.

[8] Equations (1)–(4) are solved numerically using software based on finite element package Sepran [*Cuvelier et al.*, 1986]. A markerchain method is used to incorporate the compositional buoyancy [*van Keken et al.*, 1997]. A filter is used for the calculation of the thermal field to avoid the overshooting problem for the region surrounding the plume head [*Lenardic and Kaula*, 1993]. More details for the computation are described in Appendix A. Tests of the accuracy of our calculations for the thermochemical convection in an axisymmetric spherical shell are presented in Appendices B and C. Figure 1 shows the geometry and the finite element mesh we used for models with strongly temperature-dependent viscosity as well as some models with moderately temperature-dependent viscosity (mesh 1). The average resolution of regular elements is about 8 km. The resolutions of elements are refined to be ~2–5 km for regions near the plume axis and the bottom. The grid point spacing is half that of the quadratic elements. We assume a Newtonian fluid and the viscosity is defined by

$$\eta = \eta_0 \exp(-b\, T) \tag{6}$$

where b = log(10^n) and n is varied from 0 (isoviscous) to 3 (maximum viscosity contrast $\Delta\eta$ = 1000).

[9] The surface and the core-mantle boundary are represented by isothermal boundaries. The side wall is insulating. The initial temperature distribution is homogeneous throughout the mantle, except for a 130-km thick thermal boundary layer at the bottom with a perturbation in the region near the pole. The mechanical boundary condition for the bottom is free-slip. To isolate the physics of the formation of plumes, we impose the no-slip boundary condition on the top and the side wall to reduce the large-scale convection and the secondary instabilities in the calculation domain. Our tests show that the general features for models with a wider calculation domain (90 degrees) are similar to those in our paper (45 degrees) except that the secondary instabilities can develop earlier in the regions other than the initial thermal perturbation. It shows that the boundary is far enough and the choice of the boundary condition should not influence our conclusions. We will keep the ambient mantle viscosity and temperature contrast between CMB and mantle fixed (Table 1). We assume that the distinct composition is a mixture of various proportion between the eclogite and the ambient mantle material. The reference density profile of the eclogite is $\Delta\rho_0$ denser than the ambient material throughout the mantle, except that it is $0.5\Delta\rho_0$ denser between 400–670 km depth and $\Delta\rho_0$ lighter than the surrounding mantle between 670–1000 km depth. For eclogite the density contrast $\Delta\rho_0$ is estimated to be 200 kg/m^3 [e.g., *Christensen and Hofmann*, 1994; *van Keken et al.*, 1996; *Ono et al.*, 2001; *Lin and van Keken*, 2005]. We will assume that variable proportions of the eclogite are mixed in with ambient mantle and we will use $\Delta\rho_0$ as a

free parameter that ranges from 0 to 400 kg/m^3. While this is larger than that based on a 100% eclogite composition, it will allow us to better understand the sensitivity of our modeling results to the density contrast.

3. Results

[10] We will first present the models for plumes formed by purely thermal origin as a reference. The thermochemical model results that follow can be categorized into two end-member regimes (regimes I and II) and an intermediate regime (regime III) [*Lin and van Keken*, 2005]. We will show the representative cases to demonstrate the general characteristics of the plumes that originate from a thermochemical boundary layer and the entrainment of a dense layer by plumes. We then show the influence of the properties of the compositional layer and the viscosity on the entrainment process and temperature and upward velocity of plumes. We will show snapshots of the evolution of the plumes and indicate the dimensional time, using the dimensional parameters of Table 1. For clarity we show the mirror image of the plume as well. We will use a range of dimensional values for parameters such as thickness, density contrast and temperature contrast that we think is reasonable for the properties of the D″ layer. The models can be compared with published models by converting the dimensional parameters into the buoyancy number, $B = \Delta\rho/\rho\alpha\Delta T$, where $\Delta\rho$ is the intrinsic density difference between the dense layer in the lowermost mantle and the overlying mantle; for reference, the thermal boundary Rayleigh number in our calculations based on the dimensional values in Table 1 is $Ra = 2.1 \times 10^6$. Noted that Ra is based on the assumed values for temperature increase across the boundary layer (750 K) and lower mantle viscosity 10^{22} Pa · s. Both the temperature increase across the D″ layer and the average ambient lower mantle viscosity are potentially higher. On the basis of present-day estimates for these values we can assign a factor of 2–3 uncertainty to Ra. As we will show below the sensitivity of the dynamics to the chemical density contrast and in particular the temperature dependence of viscosity is much stronger, and we have chosen to keep the Rayleigh number constant in this series of experiments.

3.1. Plumes With Purely Thermal Origin

[11] The centerline temperature of the plumes is approximately as high as the maximum thermal perturbation of thermal boundary layer (Figure 2). In addition, flow in the plume axis is strong due to the convergence at the pole which results in thickening of the thermal boundary layer [*Leitch et al.*, 1996]. The mobility of the plume material is constrained by the viscosity of the surrounding mantle. The coupling within the plume becomes weaker and the plume tail becomes thinner when the viscosity contrast increases (Figures 2b and 2c). The velocity in the plume axis is significant faster in the variable viscosity models. The plume conduit can provide hot material to the plume head more efficiently. This increases the volume of the plume head and therefore the upward velocity of plume head significantly. The morphology of the plume heads changes from sprout- to mushroom-shaped when viscosity contrast increases as shown in previous studies [e.g., *Griffiths and Campbell*, 1990; *van Keken*, 1997; *Kellogg and King*, 1997; *Bercovici and Kelly*, 1997]. The general features are consistent with the models with the same geometry by *Kellogg and King* [1997], except that the development of plume is faster and the effect of diffusion is smaller for the models with variable viscosity in our calculation. The differences can be attributed to the differences in rheological description.

3.2. End-Member Regimes

[12] Representative models for the evolution of the plumes and the entrainment of a dense layer in the end-member regimes I and II are shown in Figure 3. When the excess density of the compositional layer is large enough the dense material prevents the lowermost portion of TBL to participate in the formation of the plume (regime I) (Figures 3a and 3b). The plume head is formed by the material originally a few tens of kilometers above CMB. The plume temperature is therefore generally much lower than the total temperature increase across the TBL as was noted earlier by *Farnetani* [1997]. Only a negligible amount of the dense material is entrained by the thermal plumes. The upward velocity is much lower because of its lower temperature.

[13] When the thermal effect dominates the plume formation, plumes entrain a substantial volume of the dense material and the centerline temperature remains high (regime II). The presence of the dense layer lowers the net buoyancy force of the plume and slows its upward motion compared to the purely thermal case. The shape of the plume is generally significantly distorted. For the isoviscous plume model with $d = 150$ km, $\Delta\rho = 50$ kg/m^3, $B = 0.56$ (Figure 3c), it forms a root with a wide radius

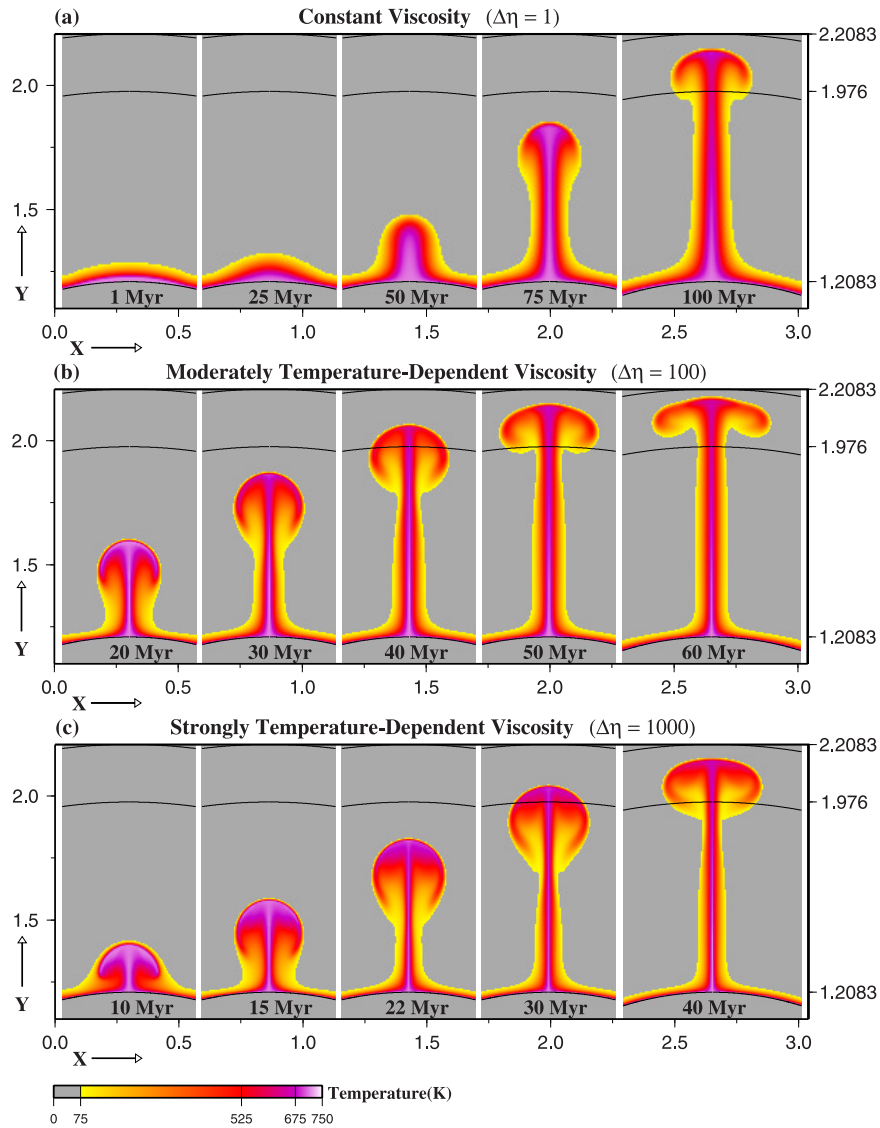

Figure 2. Plume models with purely thermal origin in an axisymmetric spherical shell geometry. Length scale is rescaled by the thickness of the mantle (2885 km). The nondimensional values marked on the right axes (1.2083, 1.976, 2.2083), and the corresponding black lines at three depth levels represent the CMB, the 670-km discontinuity, and the surface, respectively. The same notation is used throughout the paper.

in the lower mantle during about 250–320 Myr. In the model with temperature-dependent viscosity (Figure 3d: $\Delta\eta = 100$, $d = 100$ km, $\Delta\rho = 50$ kg/m^3, $B = 0.56$) the temperature of the plume center is much higher than the rest of plume head with resultantly higher velocity. The shape of the plume head is stretched during its ascent because of the significant difference of upward velocity between the plume center and the rest of the plume head.

3.3. Intermediate Regime: Regime III

[14] For isoviscous models, the flow field is basically dominated by the concentric flow drawn to the plume [*Zhong and Hager*, 2003]. However, the complexity of the entrainment process and the plume formation gradually increases with the increase of viscosity contrast and we see the development of complicated behavior, that falls between the two end member regimes. Figure 4 shows an example where the thermal effect still dominates the plume formation but the intrinsic density contrast affects the entrainment ($\Delta\eta = 100$, $d = 25$ km, $\Delta\rho = 100$ kg/m^3, $B = 1.11$). The concentric flow draws the material of TBL to the axis. The dense material prevents the development of plume head from the lowermost portion of TBL where the dense material presents. Most of the

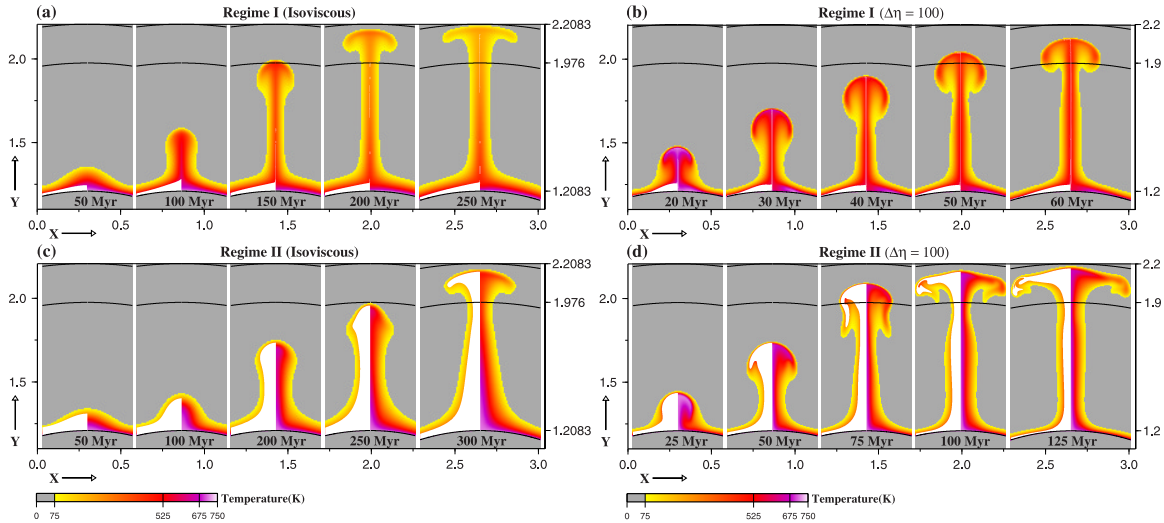

Figure 3. Representative models showing the evolution of plumes in regimes I and II with isoviscous rheology: (a) regime I: $\Delta\rho = 300$ kg/m^3, $d = 50$ km, $B = 3.33$ and (c) regime II: $\Delta\rho = 50$ kg/m^3, $d = 150$ km, $B = 0.56$, and moderately temperature-dependent viscosity: (b) regime I: $\Delta\rho = 200$ kg/m^3, $d = 25$ km, $B = 2.22$; (d) regime II: $\Delta\rho = 50$ kg/m^3, $d = 100$ km, $B = 0.56$. The white color marks the distribution of the dense material. The notation for the compositional field is used throughout the paper.

dense material accumulates around the foothold of plume and induces a counter circulation [e.g., *Kellogg and King*, 1993; *Christensen and Hofmann*, 1994; *Farnetani*, 1997]. Only a negligible amount of dense material is entrained by the plume head and it forms a thin tendril in the plume axis at the earlier stages (e.g., Figure 4, 20 Myr, 40 Myr). This feature is commonly observed in the models with temperature-dependent viscosity and a relatively thin ($\sim\leq$50 km) and heavy ($\sim\geq$50 kg/m^3) dense layer. The pile-up of the dense material at the base of the plume and the entrained material in the plume conduit caused by the high buoyancy number is similar to that observed by *Jellinek and Manga* [2002]. The shape of the plume head is similar to that of the purely thermal plume, but the internal plume structure is modified. A considerable volume of dense material is entrained until its temperature becomes high enough so the net buoyancy of this material parcel is positive. The viscosity of the dense material is low due to the high temperature. This allows the material to be sheared and to be detached from the dense layer. The velocity of this parcel is higher than that of the plume head. This is caused by a combination of effects of (1) the deceleration of the plume head by the effect of the top surface, (2) the entrained dense material traveling along the preexisting, low-

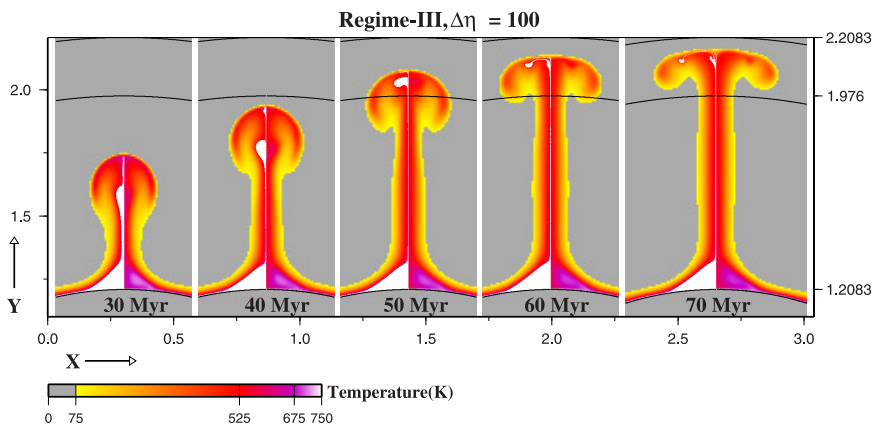

Figure 4. The entrainment of the dense material shows a transient behavior in the transitional regime (regime III). Both the temperature and composition are heterogeneous in time and space. The entrained dense material has a higher temperature in general. Model parameters for this calculation: $\Delta\eta = 100$, $\Delta\rho = 100$ kg/m^3, $d = 25$ km, $B = 1.11$.

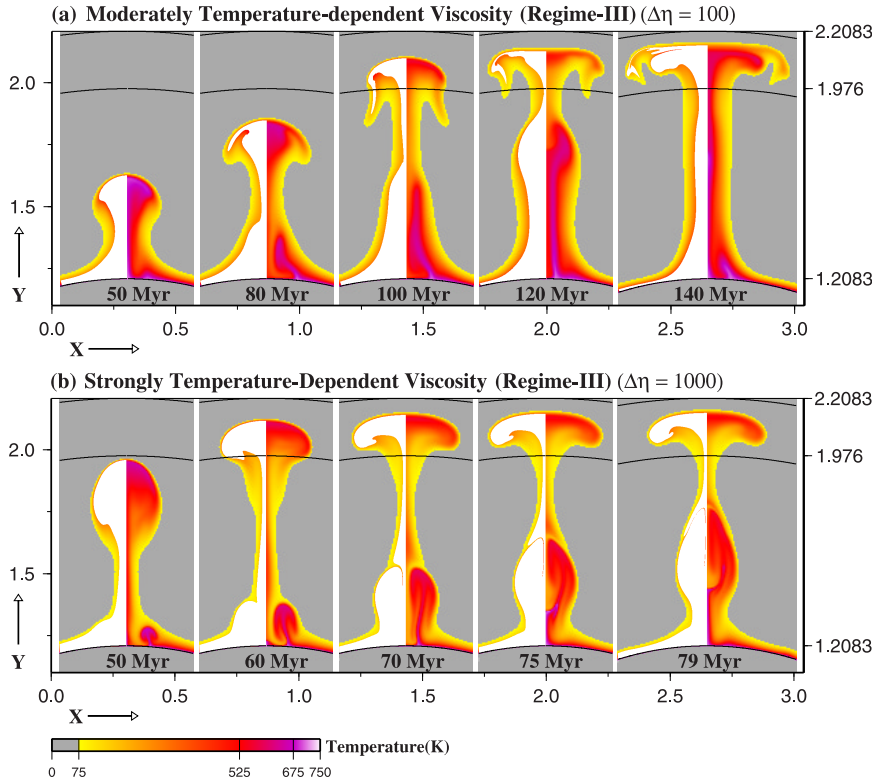

Figure 5. Representative models showing the development of secondary instabilities (regime III). Model parameters: (a) $\Delta\rho = 60$ kg/m^3, $d = 100$ km, $\Delta\eta = 100$, $B = 0.67$; (b) $\Delta\rho = 40$ kg/m^3, $d = 150$ km, $\Delta\eta = 1000$, $B = 0.44$.

viscosity conduit, and (3) the density inversion of the entrained material in the mid-mantle. It reaches the top of the plume head and then migrates away from the plume axis. The compositional density causes a form of small-scale convection in the plume head away from the axis. This process generates the spatial and temporal heterogeneity of both the temperature and compositional fields.

[15] When the volume of the dense material in the region of contour circulation increases, the lower portion of TBL is entrained into the upper portion of the TBL by the counter flow. It increases the temperature of the accumulated material near the base of the plume axis and eventually induces the development of secondary instabilities when the compositional and thermal effects are compatible [*Lin and van Keken*, 2005] (Figure 5). The development of the secondary instabilities becomes a common feature in the models with strongly temperature-dependent viscosity.

3.4. Another "Regime": No Plume

[16] When the dense layer is sufficiently thick or dense, the formation of the plume is strongly retarded or completely prohibited. We consider the plume formation prohibited if the plume that is formed from the initial thermal perturbation does not reach the subsurface region within 300 million years in our models. In the case of constant viscosity, models with a thickness of the dense layer that is similar or larger than that of the thermal boundary layer ($\sim \geq 100$ km) show that a large portion or even the entire TBL is prohibited from developing plumes (e.g., isoviscous model, $\Delta\rho = 200$ kg/m^3, $d = 200$ km, $B = 2.22$). The temperature of the TBL increases slowly and the thickness of TBL gradually becomes thicker mainly by conduction in time when the formation of plume is initially suppressed. The upper portion of the TBL eventually is able to move laterally toward the central axis and gradually increases the thermal perturbation near the pole when the thickness of TBL becomes thicker by conduction. This forms an unsteady stagnation streamline, which separates the upper portion and the lower portion of the TBL as that in models of regime I. In some models with high-density contrast, small-scale convection occurs and counter flows develop in the middle portion of the TBL. In a particular case, the counter circulation separates the upper portion and the lower portion of TBL in a transient matter during

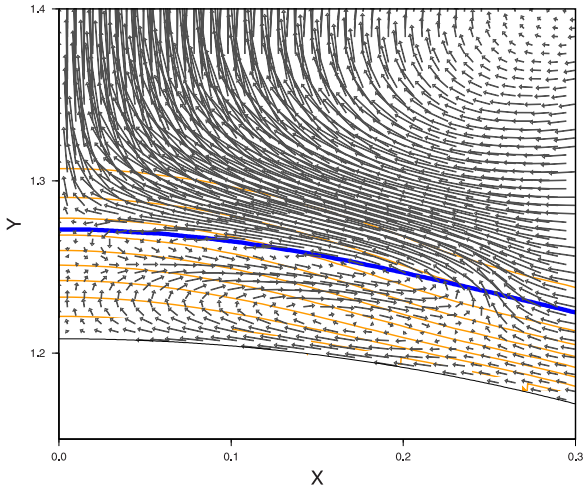

Figure 6. Flow field showing counter circulation in the upper portion of a thick, heavy dense layer for an isoviscous model of snapshot at 80 Myr. The blue line outlines the upper boundary of the dense layer, and the yellow lines show the nondimensional thermal field with contours of 0.1–0.9 with interval of 0.1.

~60–130 million years (Figure 6: isoviscous, d = 150 km, $\Delta\rho$ = 150 kg/m^3, B = 1.67). The circulations then emerge with the lower portion of the TBL to be a large, sluggish counter circulation in the middle-lower portion of the TBL near the pole at ~130 million years. Eventually, a plume with temperature about only less than 15% of maximum excess temperature is formed when the TBL is developed to be thicker after about 300 million years, which would not survive as a mantle plume in the convective mantle. We assume that under these conditions the thermal boundary layer cannot generate plumes.

3.5. Entrainment of a Dense Layer

[17] Figure 7 shows the entrainment as a function of the excess density and the thickness of the compositional layer. The entrainment is characterized by the total volume of the entrained dense material in the upper mantle (V_e) as it evolves over time. For isoviscous models, the entrainment is sensitive to the excess density and thickness of the compositional layer. High-temperature thermochemical plumes in regime II can be generated even when the intrinsically excess density of the dense layer is much higher than the maximum negative density variation due to the thermal expansion (−90 kg/m^3) if the layer is thin enough (e.g., $\Delta\rho$ = 250 kg/m^3, d = 10 km, B = 2.78). The entrainment is more sensitive to the density contrast for the models with temperature-dependent

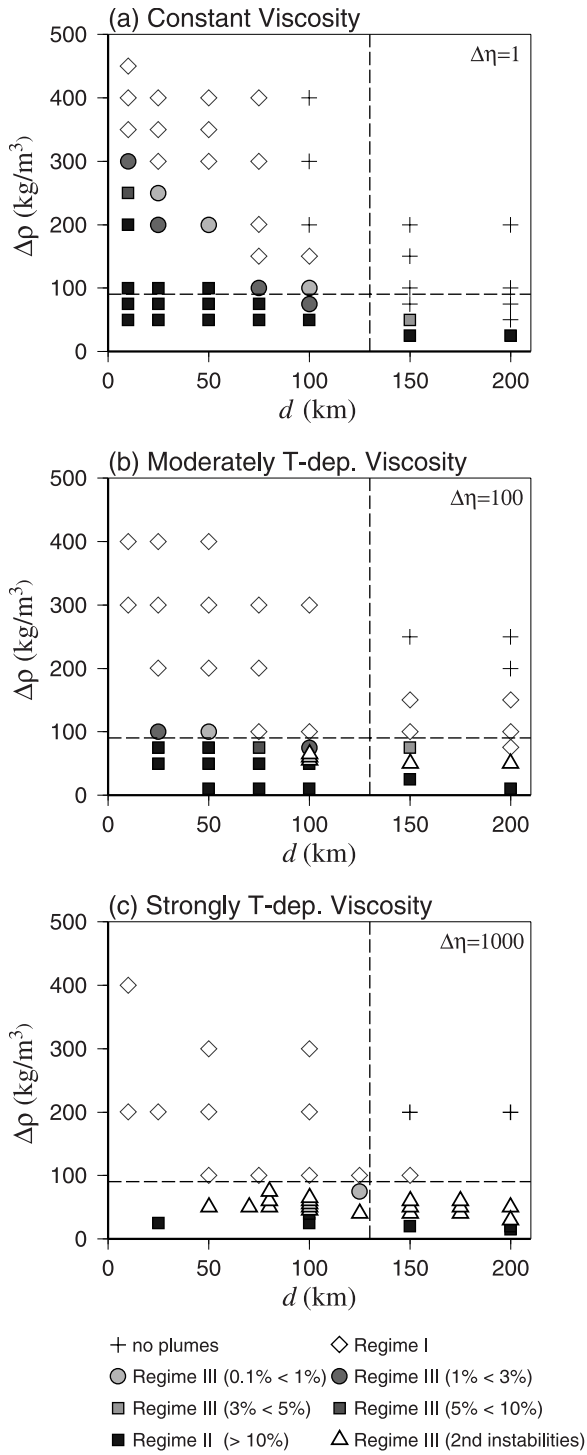

Figure 7. Entrainment as a function of viscosity contrast, intrinsic density contrast, and thickness of the compositional layer. Vertical dashed lines depict the thickness of the initial thermal boundary layer (130 km). Horizontal dashed lines mark the maximum density variation due to thermal expansion (−90 kg/m^3) in our models.

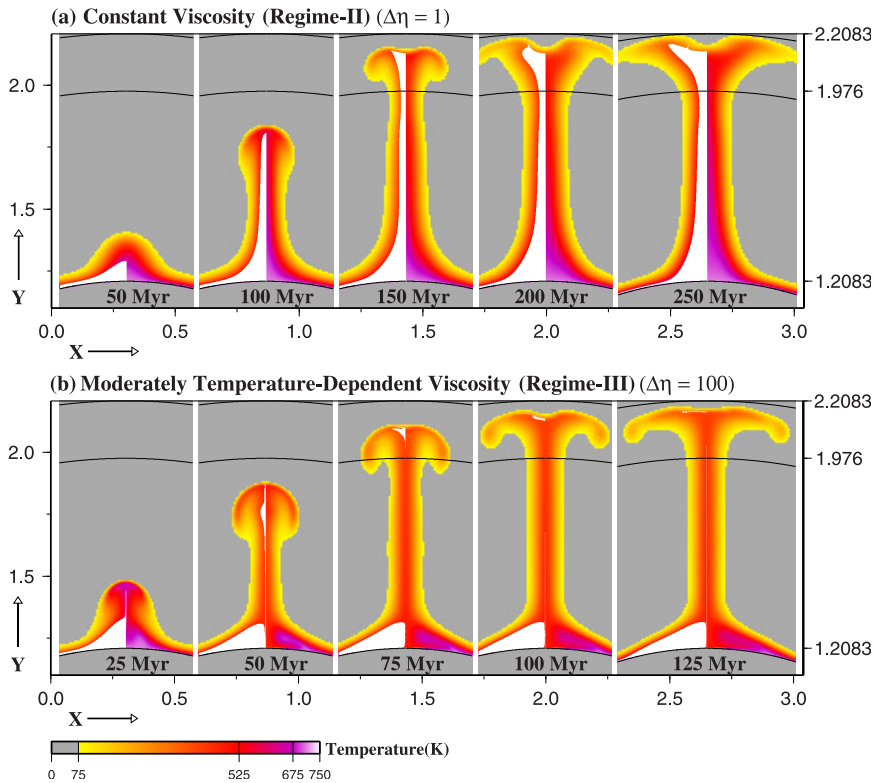

Figure 8. Example for the comparison of the entrainment and evolution of plume between the isoviscous model (regime II) and model with moderately temperature-dependent viscosity (regime III) for a calculation with $\Delta\rho$ = 100 kg/m^3, d = 50 km, B = 1.11. The volume of the entrained dense material is significantly lower in the models of variable viscosity mainly due to the weaker mechanical coupling.

rheology. The strong coupling between the dense material and the surrounding mantle in the isoviscous models allows the plume to entrain more dense material than that in the models with temperature-dependent viscosity in which the mechanical coupling becomes weaker, as proposed by previous studies [*Sleep*, 1988; *Zhong and Hager*, 2003]. Figure 8a shows the significant volume of the entrainment of the dense layer (d = 50 km, $\Delta\rho$ = 100 kg/m^3, B = 1.11) in the isoviscous models. By contrast, only a small amount of the dense material is entrained in the corresponding model with temperature-dependent rheology (Figure 8b).

[18] For isoviscous models, the temperature of the TBL slowly increases with time mainly by conduction if the dense material prohibits the formation of plume from the lower portion of TBL. For the temperature-dependent rheology models, small-scale convection with the length scale on the order of the thickness of TBL occurs in the TBL. It elevates the temperature of the upper portion of the TBL and homogenizes the thermal structure of TBL. The lower portion of the TBL feeds the plume conduit after the original plume head is established and elevates the temperature of plume axis in those cases where the upward motion of the high-temperature material is not suppressed by the counter-circulation near the plume axis. In addition, the weaker mechanical coupling in the variable viscosity models reduces the entrainment and the net buoyancy is mainly determined by the thermal effects alone. The weaker coupling also makes the separation between the upper and lower portions of the TBL easier. These mechanisms combined make it easier to generate plumes in regime I for models with temperature-dependent rheology.

[19] The dense layer influences the plume formation and hence the radius and temperature of plume. The radius of the plume conduits is often much wider than that of purely thermal plumes. The dense material is entrained approximately with a constant rate when the effect of the compositional buoyancy is minimal. The entrainment rate commonly varies with time when the compositional

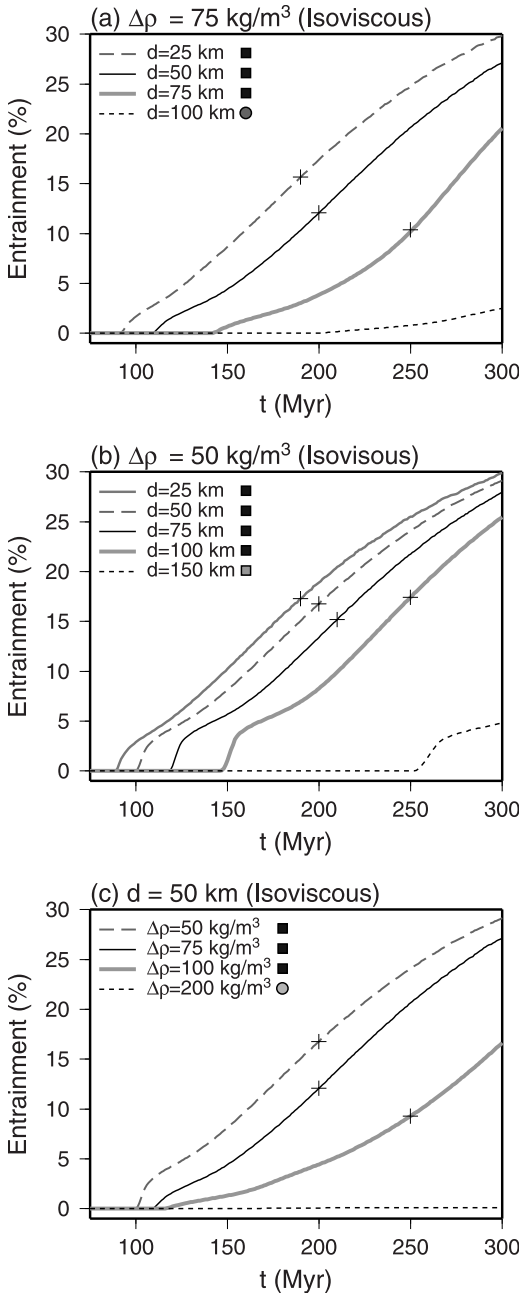

Figure 9. Time evolution of entrainment for selected isoviscous models. Crosses roughly mark the age of the initiation of the instabilities in the regions other than the initial thermal perturbation near the pole. The same symbols as in Figure 7 are used to indicate which regime each model is in.

buoyancy plays a role. The representative cases for the time evolution of V_e for isoviscous models and models with moderately temperature-dependent viscosity are shown in Figures 9 and 10, respectively. In general, V_e increases rapidly at first which corresponds to the arrival of the plume head in the upper mantle. Eventually, instabilities in the TBL will be induced in the regions other than the initial thermal perturbation near the pole. The flow field and V_e are modified after the formation of another plume. Of interest here is the length of time between the establishment of the primary plume head in the subsurface region and the initiation of another plume in regions other than the initial perturbation (Figures 9 and 10). For isoviscous models, V_e increases linearly (e.g., $\Delta\rho = 50$ kg/m^3, $d = 50$ km, $B = 0.56$) or gradually increases (e.g., $\Delta\rho = 75$ kg/m^3, $d = 100$ km, $B = 0.83$) (Figure 9). For the models with moderate viscosity contrast, various slopes of the evolution of V_e are observed (Figure 10). The slope eventually becomes zero if only a single blob of dense material is entrained (e.g., $\Delta\rho = 75$ kg/m^3, $d = 100$ km, $B = 0.83$). The slope changes from concave upward to concave downward after it reaches the subsurface region when the development of the plume conduit starts to show transient behavior (e.g., $\Delta\rho = 50$ kg/m^3, $d = 100$ km, $B = 0.56$). The entrainment becomes multiple stages in response to the pulses of material flux if the secondary instabilities develop (e.g., $\Delta\rho = 50$ kg/m^3, $d = 150$ km, $B = 0.56$). The characteristics of the entrainment for the models with strongly temperature-dependent viscosity are similar to those in the models with moderately temperature-dependent viscosity, except that entrainment with multiple stages is the dominant feature.

3.6. Average Plume Temperature and Vertical Velocity

[20] The average plume temperature and velocity are calculated by averaging the values along the plume axis in the upper mantle when the plumes reach the surface. The presence of the chemical stratification in the lowermost mantle considerably influences the plume temperature, but does not always lead to a low temperature plume (Figure 11). The plume temperature depends on both the excess density and the thickness of the dense layer when $\Delta\rho \leq 100$ kg/m^3 ($B \leq 1.11$). The plume temperature is primarily sensitive to the thickness when $\Delta\rho \geq 100$ kg/m^3. The upward velocity is general significantly lower than those of the pure thermal plumes (Figures 2, 3, and 12). The lower temperature of the plumes in regime I and the presence of the intrinsically dense composition within the plumes in regime II both reduce the total net buoyancy force of plumes. The average upward velocity of the plumes axis in the upper mantle is less than 5 cm/yr when the excess density is greater than $\sim$75 kg/m^3 or the thickness is larger

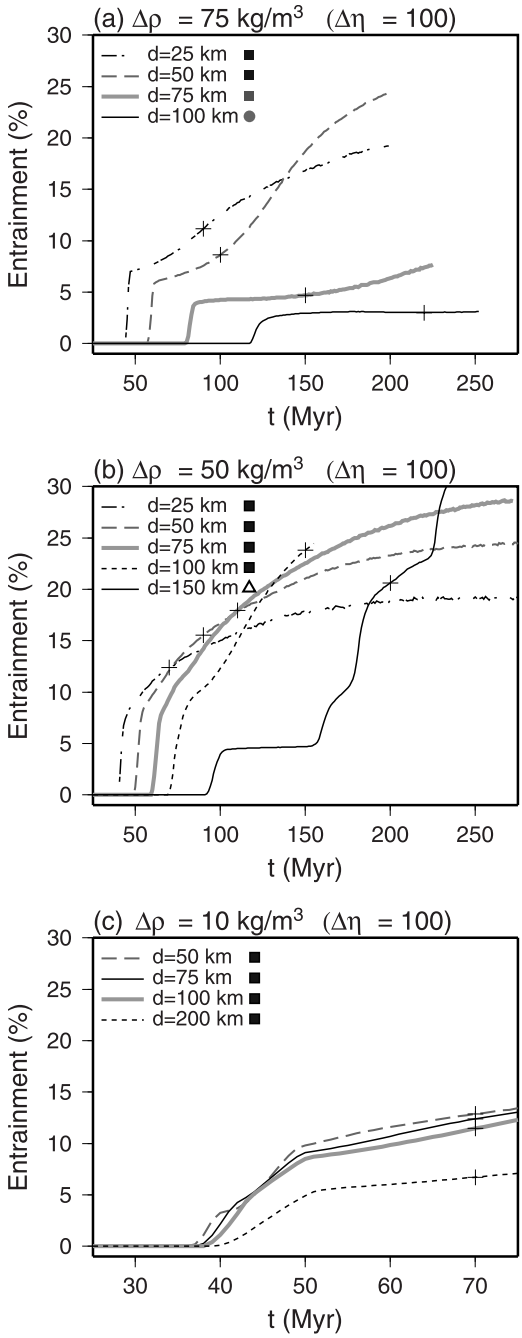

Figure 10. Similar to Figure 9, except for models with moderately temperature-dependent viscosity ($\Delta\eta = 100$).

than 50 km for the model with moderate viscosity contrast.

4. Discussion and Conclusions

[21] We have identified three separate regimes of plume formation from a thermochemical boundary layer. The parameter boundaries between these regimes are sensitive to the density and thickness of the compositional layer and the temperature dependence of the viscosity. For isoviscous models there is a direct trade-off between thickness of the layer and its compositional density. For strongly temperature-dependent models, which we consider more realistic, the density is the main parameter controlling the dynamics. If the compositional density is larger than the thermal buoyancy plumes will not form or entrain only small amounts of dense material. If the compositional density is much smaller than the thermal buoyancy the dense layer is nearly completely entrained which may lead to a reduced velocity and plume head temperature compared to the purely

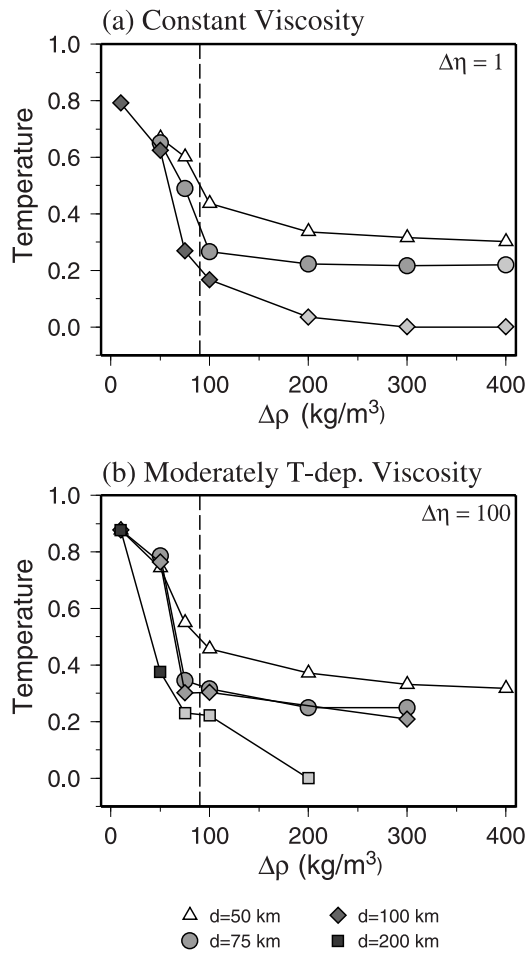

Figure 11. Average temperature of plume axis in the upper mantle as a function of the intrinsic density contrast and thickness of the dense layer. Temperature is normalized by maximum thermal perturbation (750 K). Symbols with a lighter color represent models where the plume does not reach the surface within 300 million years and the results are obtained by averaging the temperature along the plume axis in the upper mantle for the snapshot of 300 Myr. Vertical dashed lines mark the maximum density variation due to thermal expansion (-90 kg/m^3) in our models. Similar notation is used in Figure 12.

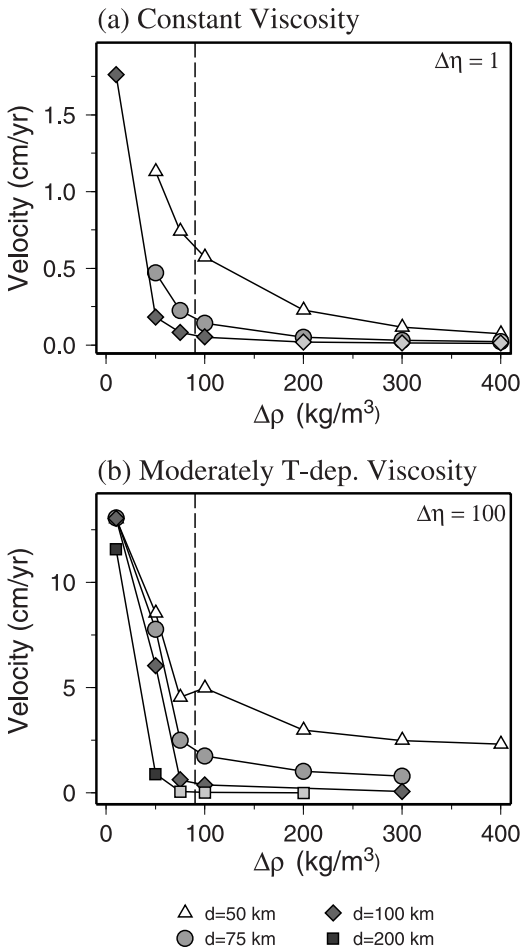

Figure 12. Average vertical velocity along the plume axis in the upper mantle as a function of intrinsic density contrast and thickness of the dense layer. The average velocity is much lower than the upward velocity of plume head because the propagation slows down when it approaches the surface. Symbols with a lighter color represent the models where the plume does not reach the surface within 300 million years.

thermal case. If the compositional density is intermediate between these two end-member regimes we find complex episodic flow of thermal instabilities up the preexisting plume conduit.

[22] Two-dimensional Cartesian models show that a dense layer with about 1200 kilometer thickness is dynamically stable if its intrinsic density is 4% higher than that of the overlying mantle [*Kellogg et al.*, 1999]. *Zhong and Hager* [2003] using axisymmetric spherical isoviscous models show that 90% of the dense layer can survive the history of the Earth if the net negative buoyancy is 1% and the thickness of the dense layer is 1000 km. We could extrapolate from these conclusions the consequences for our models in which we consider the stability for a compositionally dense layer of 10–200 km at the lowermost mantle. Our model results show that only less than 0.1% of the dense layer will be entrained into the plume within 300 million years when the intrinsic density contrast is larger than about 2% for variable viscosity models. In this case, the dense layer in D″ would be a persistent feature over significant time. When the intrinsic density contrast is less than about 1%, the dense layer in the lowermost mantle in the model domain will be almost consumed completely at the time scale of ~100–1000 million years. In this case, the survival of the thermochemical boundary layer at D″ may require constant recharge of the dense layer or chemical stratification within the boundary layer. For a compositional layer with an intrinsic density increase of about 1–2%, the survival of the dense layer in the time scale of 1 Gyr requires replenishment in general. However, if the density contrast is greater than about 1.5% and the thickness is greater than about 75 km, the dense layer is dynamically stable in the lowermost mantle.

[23] One disadvantage of the axisymmetric spherical geometry is that the symmetric condition at the pole does not allow the plume and dense material migrate laterally, which may lead to a stronger pile-up of material. In addition, the axisymmetric geometry assumes a specific initial perturbation and the symmetrical development of the plumes. The compositionally distinct layer in the Earth's mantle is likely laterally heterogeneous. The development of the plume may be asymmetrical when the viscosity contrast is larger than about two or three orders of magnitude, even with initially symmetrical perturbation. However, the current simplification is necessary so that the extensive high-resolution calculations with variable viscosity are possible to conduct and still to be able to capture the general characteristics and to explore the entrainment in a quantitative sense. The general conclusions should hold as long as the plumes are formed in a thermal boundary layer with dense material. Tests in a full three dimensional geometry would help to further approach the real features in the deep interior of the Earth [e.g., *Farnetani and Samuel*, 2005].

Appendix A: Numerical Approaches for the Thermochemical Convection Problems in Axisymmetric Spherical Geometry

[24] We have tested both a tracer and markerchain method [*van Keken et al.*, 1997] in the primitive

variable formulation. Both methods are well suited to track the composition in a nondiffusive manner. The incorporation of the chemical buoyancy force is somewhat more involved and both methods have distinct advantages and drawbacks. In the tracer method we discretize the dense layer by a large number of uniform tracers that each carry a proportion of the excess density as point volumes $\Delta V\delta(\mathbf{x})$ where ΔV the volume of the tracer and $\mathbf{x}$ the position of the tracer. The composition function is then simply the summation over all point masses. In the finite element formulation the Stokes equation is discretized into a matrix-vector system $\mathbf{Su} = \mathbf{f}$ where $\mathbf{S}$ is the stiffness matrix, $\mathbf{u}$ the vector of (unknown) velocity components and $\mathbf{f}$ is the load vector that contains among other the contribution of the buoyancy forces. The compositional buoyancy adds an incremental load vector with components

$$f_i = Rb \int \Gamma \phi_i(\mathbf{x}) dV \tag{A1}$$

where ϕ_i is the i-th shape function and the integration is carried out over the entire domain. Due to the local support of the shape functions the assembly of the load vector is most easily carried out by evaluation of integrals only in the elements where the shape functions are nonzero. This leads to element load vectors of the form

$$f_i^e = Rb \int_e \Gamma \phi_i(\mathbf{x}) de \tag{A2}$$

which for tracers in Cartesian geometry can simply be evaluated as

$$f_i^e = Rb \int_e \sum_m \Delta V \delta(\mathbf{x}_m) \phi_i(\mathbf{x}) de = Rb \sum_m \Delta V \phi_i(\mathbf{x}_m) \tag{A3}$$

where the summation only needs to be carried out over those tracers that are in the local element. This approach can be used in axisymmetric geometry as well, although some care needs to be taken to implement the geometrical integration factor $(2\pi r)$ correctly.

[25] The implementation of the compositional buoyancy force for the markerchain method is slightly more involved since we need to extract the volume that is occupied by the dense layer from the markerchain, which only defines the interface between the dense layer and normal mantle. One encounters the same problem in extracting the location of the dense layer for graphical purposes. We have found it efficient to use a separate regular high-resolution regular grid containing a large number of "pixels." By counting the intersections with the markerchain for a given column of pixels we can color the pixels or switch them on or off, depending on whether they are above or below the markerchain. Each "on" pixel can then be considered a point mass with a similar construction of the load vector as shown above for the tracer method. We have made extensive comparisons between the tracer and markerchain methods, which logically follows previous comparative work [e.g., *van Keken et al.*, 1997; *Tackley and King*, 2003].

[26] The tracer method described above (called the "absolute tracer method" by *Tackley and King* [2003]) is straightforward, but the accuracy depends strongly on the number of tracers. There are two main drawbacks. Each tracer acts as a "Stokeslet" that may cause compaction and settling of the tracers which violates the conservation of mass. In addition, the strain that naturally builds up in the deforming medium leads to tracer compression and rarefaction, which can cause significant artificial fluctuations in the local density. These problems can be partly avoided by adding a set of neutral tracers that correspond to the fluid outside of the dense layer and using the ratio of dense to neutral tracers in the computation of the local density function, which is the basis of the "tracer-ratio method" of *Tackley and King* [2003]. While this method shows better behavior for thermochemical convection than the absolute tracer method at the same tracer resolution, there is a significant computational increase due to the need to track neutral tracers. This is a particularly strong disadvantage in the case of a compositionally distinct layer that is small compared to the size of the model domain.

[27] The markerchain method completely avoids the tracer compaction issues of the "absolute" tracer method and is much more efficient than the tracer method when the interface is relatively undeformed. The main disadvantage of the markerchain method is that over time the interface stretches with a concurrent increase in computational effort. In relevant cases, the mixing is exponential [e.g., *van Keken et al.*, 1997, 2003] and the length of the interface increases exponentially with model time, which eventually makes this method prohibitively expensive.

[28] We have found that the markerchain method is a more efficient and more accurate than the tracer

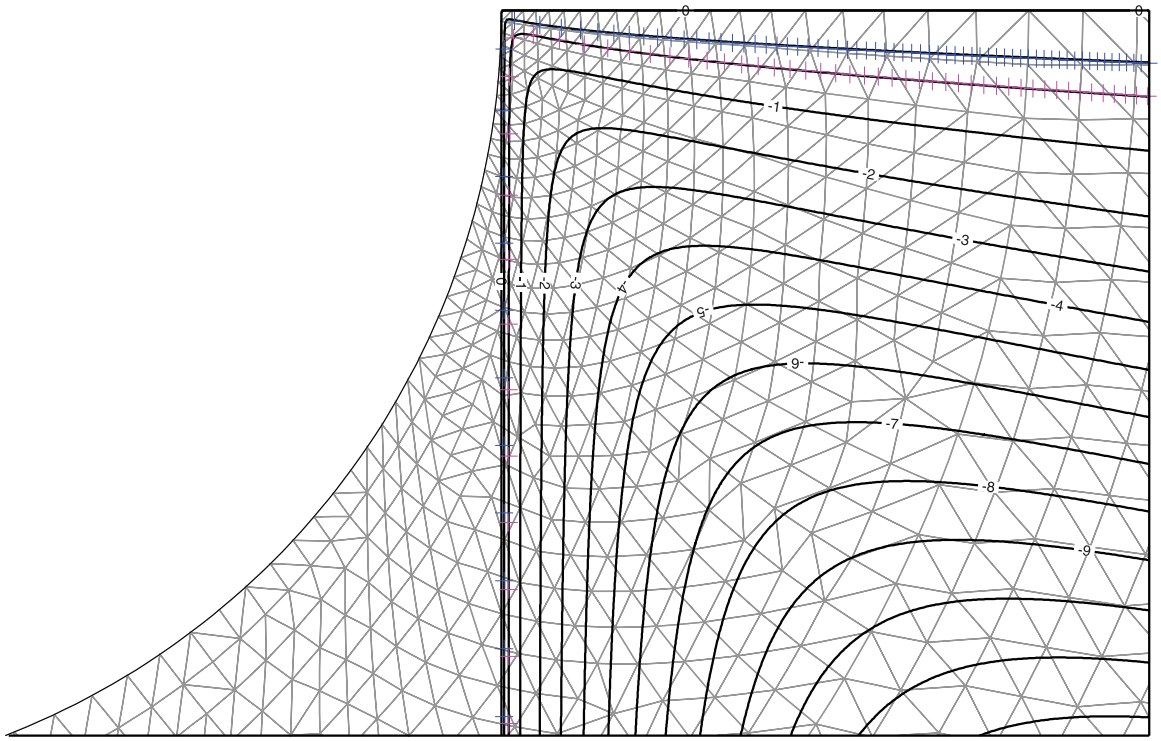

Figure B1. Comparison between the analytical solution and our model ($0 \leq x \leq 1.2083$) for the region near the corner ($0 \leq x \leq 0.4$). Particles are passively advected by the steady flow determined by the corner flow solution. Black lines represent the analytical stream function of corner flow with contours of interval = 1. Two additional contours (-0.15, -0.4) are included to show the detail near the stagnation point. Blue and purple crosses mark the traces of the particles, which were initially located on the stream function = -0.15 and -0.4 at x = 1.2, respectively. Gray lines show the elements used in this calculation. Note that figure shown here has been rotated 90° clockwise.

method for the type of models we considered here and all results presented in the paper (except for a few comparative models in Appendix B) are based on the markerchain method.

Appendix B: Benchmark Tests

[29] To validate the accuracy and robustness of the axisymmetric-spherical, thermochemical convection code, we compare our model results with both an analytical solution and published numerical solutions for two problems. The chemically distinct material is modeled using the markerchain method. The calculation relies on the accurate particle tracing and implementation of chemical buoyancy in spherical geometry. We first test the accuracy of particle tracing. Particles are advected passively in a steady state flow field determined by the analytical corner flow solution [*Batchelor*, 1967] with velocity equal to 100 at y = 0. The stream function in each marker is calculated on the basis of its location at a given time and then compared with the analytic solution. The accumulated numerical error on this relatively coarse grid is less than 0.1%, except for near the stagnation point where the stream function is not defined. The numerical error is determined by the difference between the analytic solution of the stream function and that predicted by the numerical result. Numerical errors can be further reduced by increasing element resolution. Figure B1 shows that the particle motion follows the streamline.

[30] The second benchmark problem is the entrainment of a thin dense layer by thermal convection as described by *van Keken et al.* [1997]. A similar model configuration is used by adopting the same boundary conditions and convective vigor and scaling the initial temperature field to a quarter of a sphere in axisymmetric spherical geometry. The thermal Rayleigh number is 3×10^5 and the compositional Rayleigh number is 4.5×10^5 in this calculation. Figure B2 shows an example for the evolution of the particle distribution by both the absolute tracer method and markerchain method. The initial thickness of the dense layer is 0.03. Part of the dense material piles up near the bottom, while part of dense material is entrained and mixed in the interior of the model domain. The general

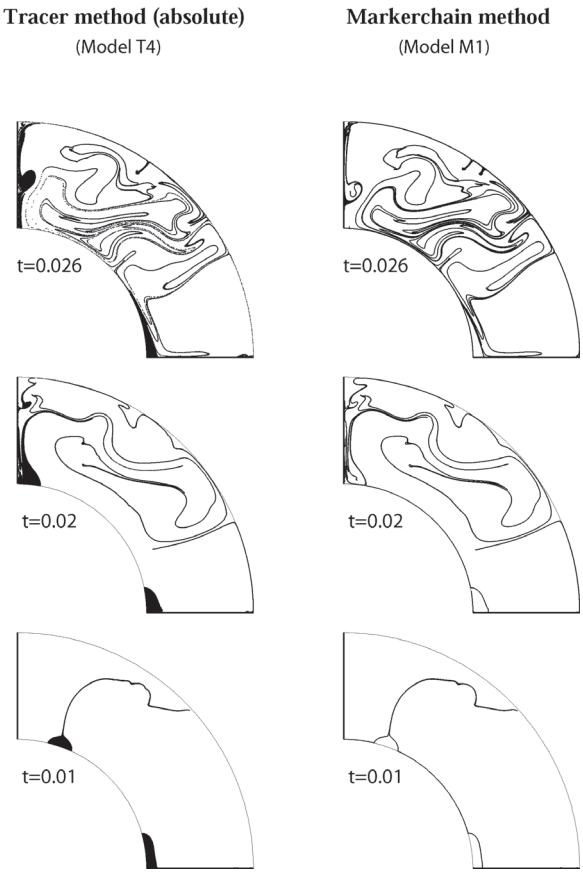

Figure B2. Compositional fields for benchmark test II using both the absolute tracer and markerchain methods.

behavior is similar to that in Cartesian geometry. The root-mean-square velocity V_{rms} is shown in Figure B3. The time evolution for cases with various resolutions is similar until $t \sim 0.012$ (~3 Gyr) for the tracer method. The rms velocity is on the same order of magnitude comparing with the thermochemical benchmark in Cartesian geometry. The entrainment is more efficient than that in the Cartesian geometry. The results obtained by using tracer method (model T4) and markerchain method (model M1) are similar if the number of the tracers is large enough, yet the continuity of the material interfaces can be modeled significantly better by the markerchain method. The density of the tracers using absolute tracer method inevitably becomes too small to accurately describe the distribution of the distinct composition after the material is stretched by large strain. Figure B4 shows the comparison of the CPU time between the model using absolute tracer method (model T4) and markerchain method model (model M1). The accumulated CPU time of model M1 increases exponentially over time due to the increase of markers in response to the increase in length of

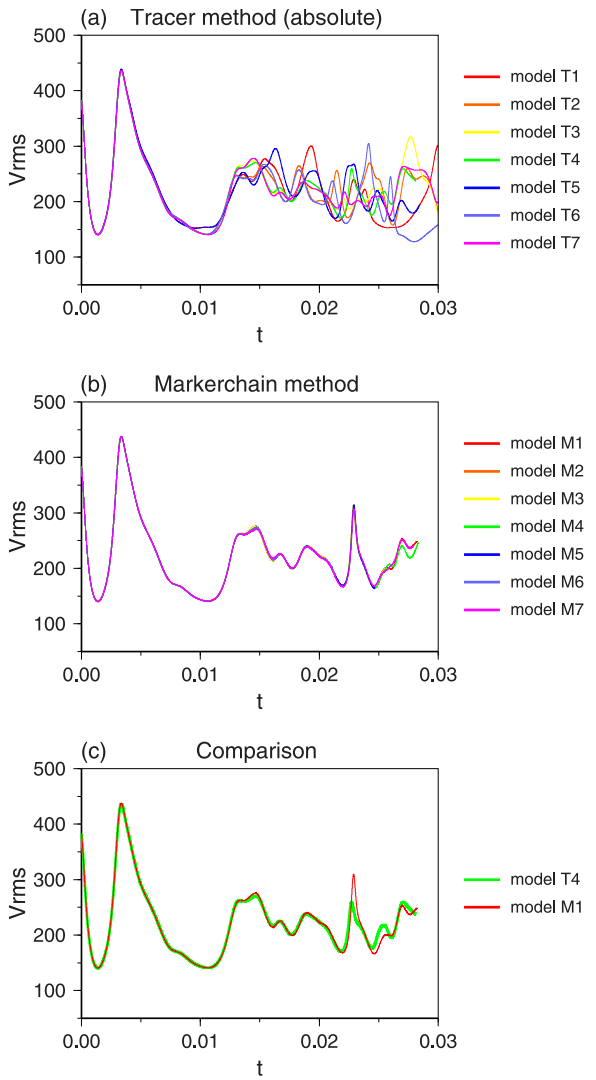

Figure B3. Evolution of rms velocity for benchmark test II. (a) Model parameters: For models T1–T4, mesh resolution ranges from 0.00625 to 0.0125. The initial intervals of tracers are 0.005, 0.002, 0.001, and 0.0005, respectively. For models T5–T7, mesh resolution = 0.005625–0.01125. The initial intervals of tracers are 0.005, 0.002, and 0.001. The evolution of the rms velocity is similar until $t \sim 0.012$. (b) Model parameters: For models M1–M3, same mesh as that in models T1–T4. The constant interval between markers are 0.005, 0.002, and 0.001, respectively. For model M4–M6, same mesh as models T5–T7. Intervals between the markers are 0.005, 0.002, and 0.001, respectively. Model M7: mesh resolution = 0.005–0.01. Interval between markers = 0.005. The evolution of rms velocity agrees well between models. (c) Comparison between models T4 and M1. The evolution of rms velocity between the results using the markerchain method and tracer method is similar only if the initial interval of the tracers is as high as ~0.0005.

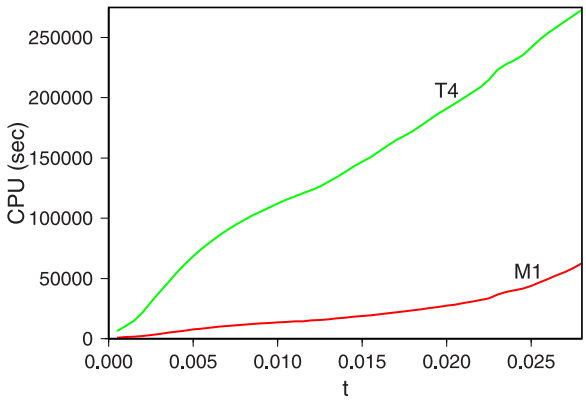

Figure B4. Comparison of the accumulated CPU time between model using absolute tracer method (model T4) and model with markerchain method (model M1).

the material interface. Nevertheless, the CPU time of model M1 is about 1/5 of that of model T4 at t = 0.025. Note that the CPU time for the tracer ratio method, assuming the same concentration of tracers, would be almost 30 times larger than that of model T4, because of the need to represent the neutral layer by tracers as well. These benchmark tests show the advantages of the markerchain method for the models we considered here.

[31] In addition to the aforementioned tests, we compare the instantaneous flow fields generated by thermal effect and compositional effect with various perturbation geometries, as well as a wide range of Rayleigh numbers. The results show good agreement between the flow fields driven by the compositional and thermal effects. The accurate calculations of the particle tracing and compositional effect as well as the good agreement of the behaviors of the dense layer entrainment with the well-tested benchmark in Cartesian coordinates make us confident of the accuracy and robustness of this code.

Appendix C: Resolution Tests

[32] We have systematically performed convergence tests to ensure the features shown in this study are reliable. Experiments of various resolutions are examined. Here we show the results with four different resolutions: (1) mesh 1: nonuniform mesh with ~2.8-km resolution at the intersection of the pole and the core, and ~8-km resolution for the regular elements (high-resolution mesh) (Figure 1), (2) mesh 2: nonuniform mesh with ~4.3-km resolution at the intersection of the pole and core, and ~9-km resolution for the regular elements (intermediate resolution mesh I), (3) mesh 3: nonuniform mesh with ~5.8-km resolution in the regions near the pole and the CMB and ~12-km resolution for the regular elements (intermediate resolution mesh II), (4) mesh4: uniform mesh with 30-km resolution (low-resolution mesh).

[33] For the isoviscous models and the models with moderately temperature-dependent viscosity in the end-member regime, the convergent tests show that even the low-resolution model (mesh 4) works well and captures the general characteristics. Both the temperature and compositional fields are similar to those in the high-resolution models. For the models with moderate viscosity contrast in the transitional regime, the low-resolution model (mesh 4) may no longer reproduce the result correctly (Figure C1). The entrainment develops earlier and the lower resolution leads to numerical instabilities such as the instabilities in the plume conduit at snapshot of 80 Myr in this particular case. However, it can still capture the general features. The result of intermediate resolution (mesh 3) is similar to the high-resolution model (mesh 1), except the temperature is slightly lower due to the numerical diffusion and it influences the entrainment mildly (Figure C1). For half of the calculations with strongly temperature-dependent viscosity, the intermediate resolution mesh (mesh 3) can reproduce the general features. However, the thermal structure and the entrainment are both influenced significantly. In addition, high-resolution mesh is required for some models in the transitional regime (Figure C2).

[34] Our resolution tests show that models with the resolution of a few tens kilometers can generally reproduce the large-scale features if the viscosity contrast is equal to or is lower than about two orders of magnitude. However, our results suggest that the calculation of thermochemical convection requires a high-resolution mesh when high-viscosity contrast is considered. Different numerical techniques may lead to different details in the model results, but the general conclusion should be similar. The calculations presented in this study are performed with two resolutions. The calculations for the isoviscous models and most of the models with moderately temperature-dependent viscosity are performed on intermediate resolution mesh II (mesh 3). The thermal plumes with purely thermal origin, models with strongly temperature-dependent viscosity and models with moderately temperature-dependent viscosity in the transitional regime are conduced on a mesh with high-resolution (mesh 1).

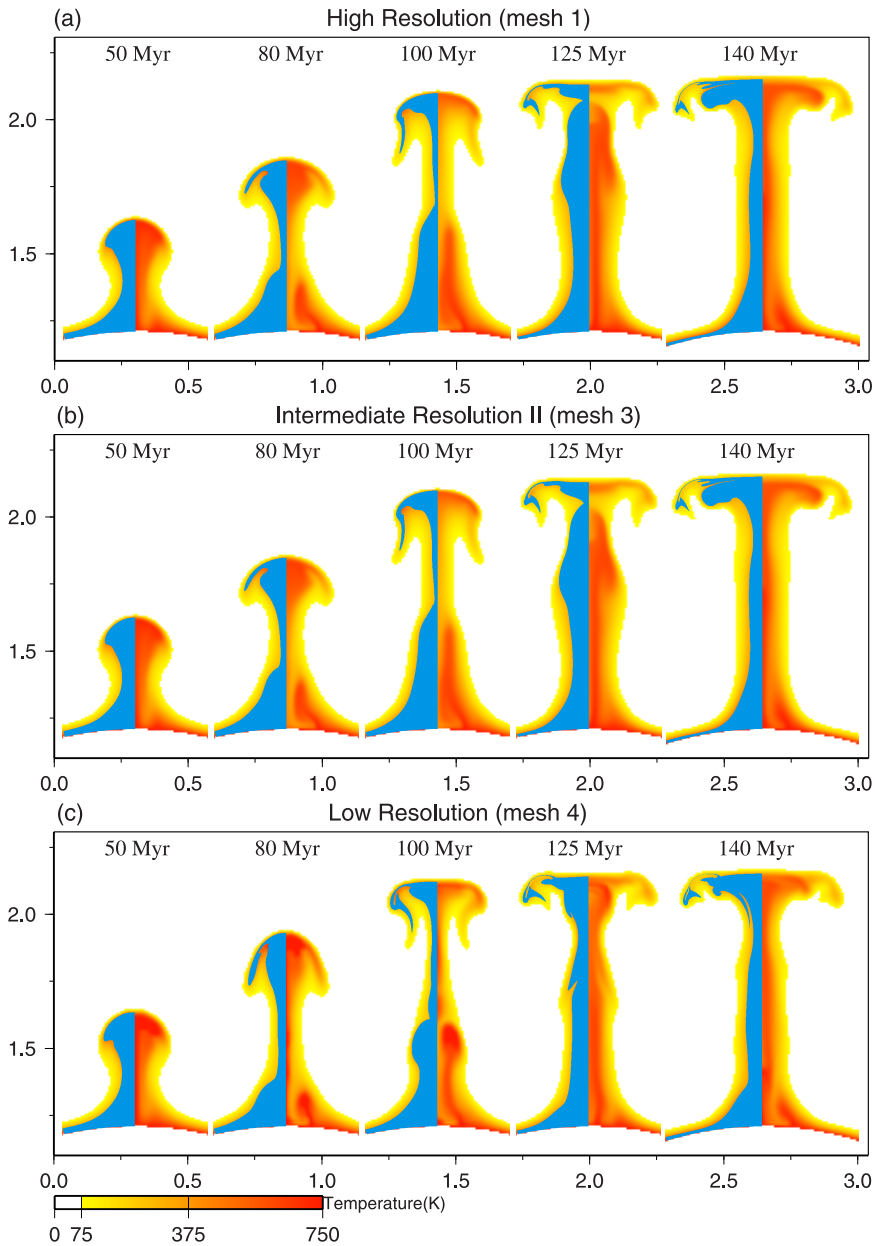

Figure C1. Example of resolution tests for models with moderately temperature-dependent viscosity ($\Delta\eta = 100$, $d =$ 100 km, $\Delta\rho = 60$ kg/m^3, $B = 0.67$) (regime III). Blue color depicts the distribution of the dense layer.

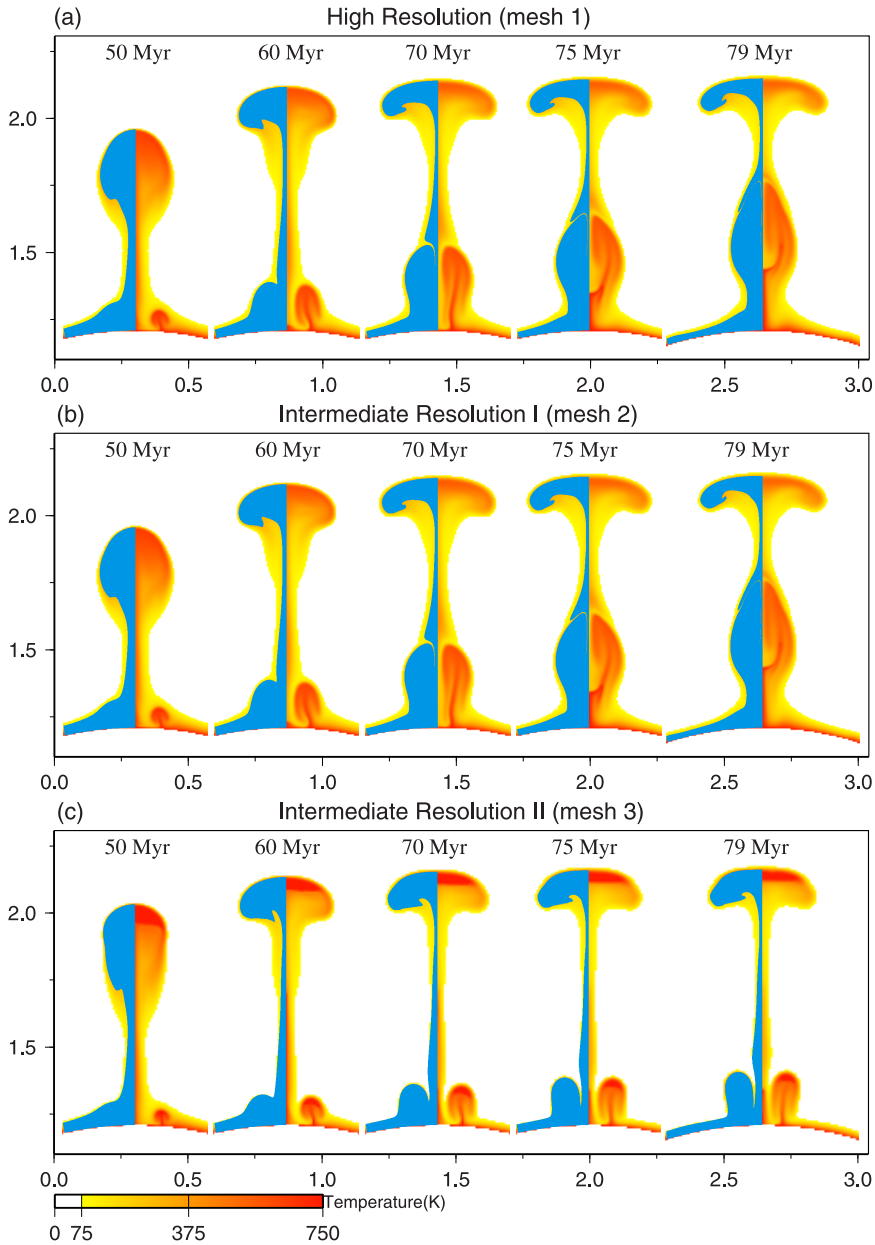

Figure C2. Example of resolution tests for models with strongly temperature-dependent viscosity ($\Delta\eta = 1000$, $d = 150$ km, $\Delta\rho = 40$ kg/m^3, $B = 0.44$) (regime III). The dense layer is marked by blue color.

Acknowledgments

[35] We thank Geoff F. Davies and Ichiro Kumagai for the constructive and helpful reviews and Magali Billen for the helpful comments and suggestions. We appreciate discussions with Cinzia Farnetani, Paul Tackley, and Shijie Zhong. This work is supported by the National Science Foundation under award EAR0229962.

References

Batchelor, G. K. (1967), *An Introduction to Fluid Dynamics*, 615 pp., Cambridge Univ. Press, New York.

Becker, T. W., J. B. Kellogg, and R. J. O'Connell (1999), Thermal constraints on the survival of primitive blobs in the lower mantle, *Earth Planet. Sci. Lett.*, *171*, 351–365.

Bercovici, D., and A. Kelly (1997), The non-linear initiation of diapirs and plume heads, *Phys. Earth Planet. Inter.*, *101*, 119–130.

Christensen, U. R., and A. W. Hofmann (1994), Segregation of subducted oceanic crust in the convecting mantle, *J. Geophys. Res.*, *99*, 19,867–19,884.

Cuvelier, C., A. Segal, and A. van Steenhoven (1986), *Finite Element Methods and the Navier-Stokes Equations*, Springer, New York.

Davaille, A. (1999), Simultaneous generation of hotspots and superswell by convection in a heterogeneous planetary mantle, *Nature*, *402*, 756–760.

Davaille, A., F. Girard, and M. Le Bars (2002), How to anchor hotspots in a convective mantle?, *Earth Planet. Sci. Lett.*, *203*, 621–634.

Depaolo, D., and G. Wasserburg (1976), Inferences about magma sources and mantle structure from variations of $^{143}Nd/^{144}Nd$, *Geophys. Res. Lett.*, *3*, 743–746.

Dziewonski, A. M., A. M. Forte, W.-J. Su, and R. L. Woodward (1993), Seismic tomography and geodynamics, in *Relating Geophysical Structures and Processes: The Jeffereys Volume*, *Geophys. Monogr. Ser.*, vol. 76, edited by K. Aki and R. Dmonska, pp. 67–105, AGU, Washington, D. C.

Farnetani, C. G. (1997), Excess temperature of mantle plumes: The role of chemical stratification across D″, *Geophys. Res. Lett.*, *24*, 1583–1586.

Farnetani, C. G., and H. Samuel (2005), Beyond the thermal plume paradigm, *Geophys. Res. Lett.*, *32*, L07311, doi:10.1029/2005GL022360.

Farnetani, C. G., B. Legras, and P. J. Tackley (2002), Mixing and deformation in mantle plumes, *Earth Planet. Sci. Lett.*, *196*, 1–15.

Fisher, J. L., M. E. Wysession, and K. M. Fischer (2003), Small-scale lateral variations in D″ attenuation and velocity structure, *Geophys. Res. Lett.*, *30*(8), 1435, doi:10.1029/2002GL016179.

Griffiths, R. W., and I. H. Campbell (1990), Stirring and structure in mantle starting plumes, *Earth Planet. Sci. Lett.*, *99*, 66–78.

Gonnermann, H. M., M. Manga, and A. Mark Jellinek (2002), Dynamics and longevity of an initially stratified mantle, *Geophys. Res. Lett.*, *29*(10), 1399, doi:10.1029/2002GL014851.

Hofmann, A. W. (1997), Mantle geochemistry: The message from oceanic volcanism, *Nature*, *385*, 219–229.

Hofmann, A. W., and W. M. White (1982), Mantle plumes from ancient oceanic crust, *Earth Planet. Sci. Lett.*, *57*, 421–436.

Hung, S., E. J. Garnero, L. Chiao, B. Kuo, and T. Lay (2005), Finite frequency tomography of D″ shear velocity heterogeneity beneath the Caribbean, *J. Geophys. Res.*, *110*, B07305, doi:10.1029/2004JB003373.

Ishii, M., and J. Tromp (1999), Normal-mode and free-air gravity constraints on lateral variation in velocity and density of Earth's mantle, *Science*, *285*, 1231–1236.

Jellinek, A. M., and M. Manga (2002), The influence of a chemical boundary layer on the fixity, spacing and lifetime of mantle plumes, *Nature*, *418*, 760–763.

Kellogg, L., and S. King (1993), Effect of mantle plumes on the growth of D″ by reaction between the core and the mantle, *Geophys. Res. Lett.*, *20*, 379–382.

Kellogg, L., and S. King (1997), The effect of temperature dependent viscosity on the structure of new plumes in the mantle: Results of a finite element model in a spherical, axisymmetric shell, *Earth Planet. Sci. Lett.*, *148*, 13–26.

Kellogg, L. H., B. H. Hager, and R. D. van der Hilst (1999), Compositional stratification in the deep mantle, *Science*, *283*, 1881–1884.

Kuo, B. Y., E. J. Garnero, and T. Lay (2000), Tomographic inversion of S-SKS times for shear wave velocity heterogeneity in D″: Degree 12 and hybrid models, *J. Geophys. Res.*, *105*, 28,139–28,157.

Lassiter, E. H., and E. H. Hauri (1998), Osmium-isotope variations in Hawaiian lavas: Evidence for recycled oceanic crust in the Hawaiian plume, *Earth Planet. Sci. Lett.*, *164*, 483–496.

Lay, T. (2005), The deep mantle thermo-chemical boundary layer: The putative mantle plume source, in *Plates, Plumes and Paradigms*, edited by G. R. Foulger et al., *Spec. Pap. Geol. Soc. Am.*, *388*, 193–205.

Lay, T., and D. V. Helmberger (1983), A lower mantle S-wave triplication and the shear velocity structure of D″, *Geophys. J. R. Astron. Soc.*, *75*, 799–838.

Lay, T., Q. Williams, and E. J. Garnero (1998), The core-mantle boundary layer and deep Earth dynamics, *Nature*, *392*, 461–468.

Leitch, A. M., V. Steinbach, and D. A. Yuen (1996), Centerline temperature of mantle plumes in various geometries: Incompressible flow, *J. Geophys. Res.*, *101*, 21,829–21,846.

Lenardic, A., and W. M. Kaula (1993), A numerical treatment of geodynamic viscous flow problems involving the advection of material interface, *J. Geophys. Res.*, *98*, 8243–8260.

Lin, S. C., and P. E. van Keken (2005), Multiple volcanic episodes of flood basalts caused by thermochemical plumes, *Nature*, *436*, 250–252, doi:10.1038/nature03697.

Lin, S. C., and P. E. van Keken (2006), Dynamics of thermochemical plumes: 2. Complexity of plume structures and its implications for mapping the mantle plumes, *Geochem. Geophys. Geosyst.*, doi:10.1029/2005GC001072, in press.

Manga, M., and R. Jeanloz (1996), Implications of a metal-bearing chemical boundary layer in D″ for mantle dynamics, *Geophys. Res. Lett.*, *23*, 3091–3094.

Masters, G., G. Laske, H. Bolton, and A. Dziewonski (2000), The relative behavior of shear velocity, bulk sound speed, and compressional velocity in the mantle: Implications for chemical and thermal structure, in *Earth's Deep Interior: Mineral Physics and Tomography From the Atomic to the Global Scale*, *Geophys. Monogr. Ser.*, vol. 117, edited by S. Karato et al., pp. 63–89, AGU, Washington, D. C.

McNamara, A. K., and S. Zhong (2004), Thermochemical structures within a spherical mantle: Superplumes or piles?, *J. Geophys. Res.*, *109*, B07402, doi:10.1029/2003JB002847.

Montague, N. L., and L. H. Kellogg (2000), Numerical models for a dense layer at the base of the mantle and implications

for the geodynamics of D″, *J. Geophys. Res.*, *105*, 11,101–11,114.
Montague, N. L., L. H. Kellogg, and M. Manga (1998), High Rayleigh number thermochemical models of a thin dense boundary layer in D″, *Geophys. Res. Lett.*, *25*, 2345–2348.
Morgan, J. P., and W. J. Morgan (1999), Two-stage melting and the geochemical evolution of the mantle: A recipe for mantle plume-pudding, *Earth Planet. Sci. Lett.*, *170*, 215–239.
Ni, S., and D. Helmberger (2003), Seismological constraints on the South African superplume: Could be the oldest distinct structure on Earth, *Earth Planet. Sci. Lett.*, *206*, 119–131.
Ni, S., E. Tan, M. Gurnis, and D. Helmberger (2002), Sharp sides to the African superplume, *Science*, *296*, 1850–1852.
Oldham, D., and J. H. Davies (2004), Numerical investigation of layered convection in a three-dimensional shell with application to planetary mantles, *Geochem. Geophys. Geosyst.*, *5*, Q12C04, doi:10.1029/2003GC000603.
Ono, S., E. Ito, and T. Katsura (2001), Mineralogy of subducted basaltic crust (MORB) for 25 to 37 GPa, and chemical heterogeneity of the lower mantle, *Earth Planet. Sci. Lett.*, *190*, 57–63.
Rost, S., E. J. Garnero, Q. Williams, and M. Manga (2005), Seismological constraints on a possible plume root at the core-mantle boundary, *Nature*, *435*, 666–669.
Samuel, H., and C. G. Farnetani (2003), Thermochemical convection and helium concentrations in mantle plumes, *Earth Planet. Sci. Lett.*, *207*, 39–56.
Sleep, N. H. (1988), Gradual entrainment of a chemical layer at the base of the mantle by overlying convection, *Geophys. J.*, *95*, 437–447.
Sobolev, A. V., A. W. Hofmann, and I. K. Nikogosian (2000), Recycled oceanic crust observed in 'ghost plagioclase' within the source of Mauna Loa Lava, *Nature*, *404*, 986–990.
Tackley, P. J. (1998), Three-dimensional simulations of mantle convection with a thermochemical CMB boundary layer: D″?, in *The Core-Mantle Boundary Region*, *Geodyn. Ser.*, vol. 28, edited by M. Gurnis et al., pp. 231–253, AGU, Washington, D. C.
Tackley, P. J. (2000), Mantle convection and plate tectonics: Toward an integrated physical and chemical theory, *Science*, *288*, 2002–2007.
Tackley, P. J. (2002), Strong heterogeneity caused by deep mantle layering, *Geochem. Geophys. Geosyst.*, *3*(4), 1024, doi:10.1029/2001GC000167.
Tackley, P. J., and S. D. King (2003), Testing the tracer ratio method for modeling active compositional fields in mantle convection simulations, *Geochem. Geophys. Geosyst.*, *4*(4), 8302, doi:10.1029/2001GC000214.
van der Hilst, R. D., S. Widiyantoro, and E. R. Engdahl (1997), Evidence for deep mantle circulation from global tomography, *Nature*, *386*, 578–584.
van Keken, P. E. (1997), Evolution of starting mantle plumes: A comparison between numerical and laboratory models, *Earth Planet. Sci. Lett.*, *148*, 1–11.
van Keken, P. E., S. Karato, and D. A. Yuen (1996), Rheological control of oceanic separation in the transition zone, *Geophys. Res. Lett.*, *23*, 1821–1824.
van Keken, P. E., S. D. King, H. Schmeling, U. R. Christensen, D. Neumeister, and M. P. Doin (1997), A comparison of methods for the modeling of thermochemical convection, *J. Geophys. Res.*, *102*, 22,477–22,495.
van Keken, P. E., E. Hauri, and C. J. Ballentine (2002), Mantle mixing: The generation, preservation, and destruction of chemical heterogeneity, *Annu. Rev. Earth Planet. Sci.*, *30*, 493–525.
van Keken, P. E., C. J. Ballentine, and E. Hauri (2003), Convective mixing in the Earth's mantle, in *Treatise of Geochemistry*, vol. 2, *Geochemistry of Mantle and Core*, edited by R. Carlson, pp. 471–491, Elsevier, New York.
Wen, L., P. Silver, D. James, and R. Kuehnel (2001), Seismic evidence for a thermo-chemical boundary at the base of the Earth's mantle, *Earth Planet. Sci. Lett.*, *189*, 141–153.
William, Q., and E. J. Garnero (1996), Seismic evidence for partial melting at the base of the Earth's mantle, *Science*, *273*, 1528–1530.
Wysession, M. E., T. Lay, J. Revenaugh, Q. Williams, E. J. Garnero, R. Jeanloz, and L. Kellogg (1998), The D″ discontinuity and its implications, in *The Core-Mantle Boundary Region*, *Geodyn. Ser.*, vol. 28, edited by M. Gurnis et al., pp. 273–298, AGU, Washington, D. C.
Zhong, S., and B. H. Hager (2003), Entrainment of a dense layer by thermal plumes, *Geophys. J. Int.*, *154*, 666–676.